

RESEARCH ARTICLE | NOVEMBER 14 2023

Effects of operational parameters on plasma characteristics and liquid treatment of a DBD-based unipolar microsecond-pulsed helium atmospheric pressure plasma jet

Min Jeong Seong; Yun Jeong Ha; Gun Hyeon Park; Sun Ja Kim ; Hea Min Joh; T. H. Chung  



Phys. Plasmas 30, 113506 (2023)

<https://doi.org/10.1063/5.0173561>



CrossMark

Physics of Plasmas

Features in Plasma Physics Webinars

Register Today!



Effects of operational parameters on plasma characteristics and liquid treatment of a DBD-based unipolar microsecond-pulsed helium atmospheric pressure plasma jet

Cite as: Phys. Plasmas **30**, 113506 (2023); doi: [10.1063/5.0173561](https://doi.org/10.1063/5.0173561)

Submitted: 23 August 2023 · Accepted: 29 October 2023 ·

Published Online: 14 November 2023





View Online



Export Citation



CrossMark

Min Jeong Seong, Yun Jeong Ha, Gun Hyeon Park, Sun Ja Kim,  Hea Min Joh, and T. H. Chung^{a)} 

AFFILIATIONS

Department of Physics, Dong-A University, Busan 49315, South Korea

^{a)}Authors to whom correspondence should be addressed: thchung@dau.ac.kr

ABSTRACT

A dielectric-barrier-discharge-based square unipolar microsecond-pulsed helium atmospheric pressure plasma jet (APPJ) was characterized by combining a simplified equivalent circuit model with a transferred charge (Q) measured by introducing an additional capacitance in series with the reactor. From Q - V plots, C_d and C_{cell} for DBD reactors under pulsed excitation were determined. Q - V plots were drawn for varying operational parameters, and the dissipated energy per cycle was evaluated. Operational parameters, such as the gas flow rate and pulse frequency, were varied, and the resulting changes in the plasma plume length, gas temperature, excitation temperature, discharge current, dissipated power, and optical emission spectra were examined. As an example of the application of the plasma jet, liquid media, including de-ionized water, were exposed to the APPJ, and their properties (pH and electrical conductivity) and concentrations of reactive species generated in the media were measured as functions of the operational parameters. Furthermore, changes in the plasma-activated media after storage for different durations and under different conditions were examined. The correlation between plasma characteristics and properties of plasma-treated liquid is discussed.

Published under an exclusive license by AIP Publishing. <https://doi.org/10.1063/5.0173561>

I. INTRODUCTION

Atmospheric pressure plasmas (APPs) have received significant attention since they are used for a variety of purpose, such as the surface modification of materials, in agriculture, and in biomedical applications (e.g., microbial inactivation, wound healing, and cancer therapy). It has been demonstrated that they can induce cell apoptosis or necrosis.¹ Among various types of APP sources, dielectric barrier discharges (DBDs) are used on an industrial scale, and they have been studied for more than a century.^{2–4} Owing to their low gas temperature, high electron energy, and the presence of active species, these discharges have high potential for use in plasma chemistry, agriculture, and water purification.⁵ Recently, atmospheric pressure plasma jets (APPJs) based on DBDs have attracted interest.^{4,6,7} In the case of such APPJs, even if the object to be treated is in contact with the plasma jet, there is no discharge current flow between the high-voltage electrode and the object.⁶ It has been found that energetically, pulsed power is much more efficient than sinusoidal power for generating a given concentration of atomic oxygen.^{8,9} In recent years, there have been

applications where pulsed-driven discharges show higher efficiency for surface oxidation or pollution removal than sinusoidal-driven discharges.^{5,9} In particular, well-defined high-voltage square pulses are employed in fundamental studies and for determining controllable and reproducible operational windows. Square pulses at low or moderate voltages have been used for generating DBDs for surface treatment and biomedical applications.^{1,10–12} For DBD systems, Q - V diagrams are used to deduce the physical properties of the discharge, irrespective of the design of the system.⁴ The form of Q - V plots for DBDs for short-pulse excitation is significantly different from the classical parallelogram.

In a recent study,¹¹ we investigated the duty-ratio-dependent phenomena in the pulsed-DBD-based APPJ treatment of liquid [de-ionized water (DW)] and polymer surfaces.¹¹ In another study,¹³ we characterized an APPJ array source driven by a bipolar voltage pulsed at several tens of kilohertz, and its electrical and optical emission characteristics were studied as functions of the applied voltage, gas flow rate, and pulse frequency.

A DBD-based APPJ was generated in a helium channel by using a square wave unipolar microsecond-pulsed voltage of low or moderate amplitude. Compared with an APPJ array, the gas flow rate for a single jet in this study was lower or moderate. The gas flow rate and the square wave features (amplitude, frequency, and duty cycle) were varied over a wide range. Q-V diagrams and other diagnostic techniques, including optical emission spectroscopy (OES), were used to deduce the physical properties of the discharges. In this study, the effects of operational parameters, such as the gas flow rate and pulse frequency, of a DBD-based APPJ on the plasma plume length, gas temperature, excitation temperature, discharge current, dissipated power, and optical emission spectra were examined.

The interaction of an APPJ with liquids has drawn increasing attention owing to the importance of the biological effects of plasma-treated liquids.¹⁴ Reactive oxygen and nitrogen species (RONS) are a key factor in plasma medicine. The chemical activity of a plasma-treated liquid is characterized by measuring the RONS concentration. The pH and electrical conductivity are also important physicochemical properties of plasma-treated liquids. In this study, DW and various cell media were employed as representative liquids, and they were exposed to an APPJ. Their physicochemical properties and concentrations of reactive species generated in the media were measured as functions of operational parameters. In particular, this study investigated the effect of operational parameters of a DBD-based APPJ on media exposed to the APPJ. The aim of this study was to determine the optimal operational parameters of the APPJ for enhancing plasma reactivity in liquid media. We also sought to elucidate the correlation between plasma characteristics and physicochemical properties of plasma-treated liquids.

II. EXPERIMENTAL SETUP

Figure 1 shows a photograph of the plasma plume generated in this study, along with a schematic of the experimental setup of the APPJ driven by unipolar high-voltage square pulses with a frequency of several tens of kilohertz (FT-Lab PDS 4000). The DBD system consisted of two electrodes. One electrode was a copper wire positioned

on the tube's axis. This electrode was electrically insulated (quartz) along its entire length, except near its end (the length of the exposed part was about 8 mm). The second (ground) electrode was a pencil-shaped ring electrode surrounded by a dielectric material (polyethersulfone). A zoom picture of the part of the dielectric channel near the nozzle with its dimension is also illustrated in Fig. 1. The gas velocity at the nozzle is in the range of 2.64 (2 SLM) to 21.2 m/s (8 SLM). Thus, the APPJ employed in this study could be considered to be a DBD jet. The APPJ source has been described in detail in our previous reports.^{1,11,12} The plume temperature was measured using a fiber-optic temperature sensor (Luxtron, M601-DM&STF), and voltage and current waveforms were obtained using a high-voltage probe (PPE 20 kV LeCroy) and a current probe (Pearson 4100). The propagation of ionization fronts was reflected in the plasma emission recorded downstream of the tube orifice. An optical spectrometer (Ocean Optics, USB-2000+XR-ES) combined with a photosensor amplifier (Hamamatsu, C6386-01) was used to determine the optical characteristics of the APPJ. The ozone concentration of the gas phase was detected using an ozone detector (2B Technologies, model202) on the basis of the absorption of 254 nm ultraviolet (UV) light. The helium gas flow rate was adjusted to be between 2 and 8 standard liters per minute (SLM) through a mass flow controller (Alicat Scientific).

In many *in vitro* studies, cells are immersed in cell culture solution. When a liquid solution is exposed to APPJ, RONS generated in the plasma phase or at the plasma-liquid interface dissolve in the liquid, resulting in a change in the characteristics, such as pH and electrical conductivity, of the solutions or distilled water. In the current study, the concentrations of long-lived reactive species, such as hydrogen peroxide (H_2O_2), nitrite (NO_2^-), and ozone (O_3), in APPJ-treated media were determined through spectrophotometry by using photoLab 7600 (WTW, Germany), by following the instructions provided by the manufacturer. The nitrite concentration was determined using the Griess reagent (Molecular Probes). Notably, physicochemical properties of the media were related to the RONS's penetration into the cellular membrane.¹⁵ The electrical conductivity and pH of the DW were measured using a conductivity stick meter (Ohaus, Starter

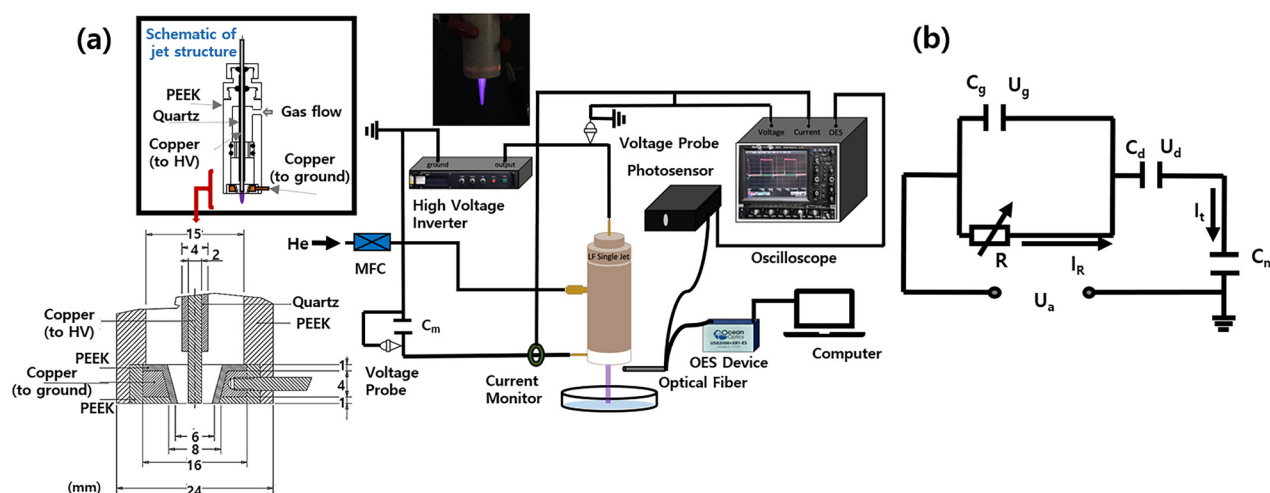


FIG. 1. (a) Schematics of the experimental setup including a zoom picture of the part of the dielectric channel near the nozzle with its dimension. (b) An equivalent circuit model.

ST3100C) and a digital pH meter (Ohaus, Starter ST3100). The distance between the nozzle and liquid surface was set to be 12 mm.

III. MODELING OF ELECTRICAL CHARACTERISTICS OF DBD DISCHARGES

A simplified model of the equivalent circuit of a DBD has been found to be useful for the electrical characterization in numerous studies.^{16–21} The equivalent circuit of a DBD cell is shown in Fig. 1(b). It has been observed that during the active discharge period, the effective capacitance of a DBD reactor is equal to the capacitance of the dielectric barriers (C_d), whereas during the dark period, it can be calculated by considering the gas gap capacitances (C_g) and C_d to be connected in series,¹⁹

$$C_{cell} = \frac{C_g C_d}{C_g + C_d}. \quad (1)$$

Several researchers have described the electrical properties of DBDs on the basis of equivalent circuit models.^{16–21} The models can be used to evaluate the DBD discharge current and gas gap voltage if the values of C_{cell} and C_d are known. The form of Q-V plots for DBDs under short-pulse excitation is significantly different from the classical parallelogram,^{2,3} and hence, it has been used to a limited extent for the accurate determination of C_{cell} and C_d .^{4,19,20}

Basically, given the values of the applied voltage $U_a(t)$ and total current $I_t(t)$, the equivalent circuit models calculate the charge $Q(t)$ on the reactor electrodes, and the capacitances C_{cell} and C_d , which can be related to other parameters of the equivalent circuit, such as the gas gap voltage $U_g(t)$, the voltage across the dielectric [$U_d(t)$], and the discharge current $I_R(t)$,^{4,18–20}

$$I_R(t) = \frac{1}{1 - \frac{C_{cell}}{C_d}} \left[I_t(t) - C_{cell} \frac{dU_a}{dt} \right], \quad (2)$$

$$U_d(t) = \frac{1}{C_d} \int_0^t I_R(\tau) d\tau = \frac{1}{C_d} Q(t), \quad (3)$$

$$U_g(t) = U_a(t) - U_d(t). \quad (4)$$

It should be noted that the sum of the charges on the reactor electrode (capacitance plates with the values of C_g and C_d), $Q(t)$, is equal to the charge transferred through the resistance R [shown in Fig. 1(b)]. Notably, the model expresses the discharge current and gas gap voltage in terms of values that can be directly measured in an experiment. The instantaneous power consumed by the plasma discharge in the discharge gap can be calculated using the equation $P_g(t) = U_g(t) \times I_R(t)$. The consideration of the equivalent circuit involves the consideration of only energy losses in the discharge, and all other types of dissipation are neglected, such as losses in the dielectric barriers or radiation.²⁰

When the discharge is not ignited, if the current measured by the current probe (i.e., the displacement current) is compared to the current predicted from the time derivative of the voltage waveform, namely, $C_{cell} \frac{dU_a}{dt}$ [in Eq. (2)], the estimation of the C_{cell} value is not easy because of a skew in time between the two signals. Measured and calculated waveforms are required to be shifted relative to each other to obtain the best fit. Furthermore, the numerical differentiation of $\frac{dU_a}{dt}$ is very sensitive to random noise and the voltage probe bandwidth.¹⁹ Therefore, instead of using Eq. (2), we sought to obtain the discharge

current by subtracting the displacement current (the current without plasma ignition) from the total current (with plasma ignition).

IV. RESULTS AND DISCUSSION

A. Plasma characterization

The transferred charge $Q(t)$ can be determined through time integration over one discharge current pulse. Furthermore, from the time development of the applied voltage $U_a(t)$ and conductively transferred charge $Q(t)$, we can draw a Q-V plot to determine discharge characteristics such as the dissipated electrical energy and the capacitances of the DBD arrangement. Such a Q-V plot is shown in Fig. 2. To obtain accurate results for pulsed-driven DBDs, we should synchronize the voltage and current signals.⁵ Since the integration of the discharge current, shown in Eq. (3), is very sensitive to small systematic errors added to the current waveform, which leads to the error increasing with time,²⁰ the measured Q-V shown in Fig. 2 (using a direct integration of I_R) contains considerable noise and shows high uncertainty.

The equivalent circuit model suggests that the discharge current can be calculated using the measured total current through the differentiation of the applied voltage [Eq. (2)], and that the transferred charge can be calculated via the integration of the discharge current [Eq. (3)]. However, this scheme was found to be impractical, especially for normal application-oriented experimental setups. Alternatively, the transferred charge can be measured by directly introducing an additional capacitance ($C_m = 10$ nF) in series with the reactor, as shown in Fig. 1.^{10,19} It should be noted that the value of C_m (nF order) is much larger than that of C_g and C_d (pF order). Therefore, C_m does not contribute to C_{cell} (and thus the equivalent circuit model). By acquiring U_{C_m} , the Q-V characteristic can be obtained when plotting $Q = C_m U_{C_m}$ vs U_a .¹⁰

Figure 3 presents Q-V plots obtained by using an additional capacitance. The values of C_d and C_{cell} can be estimated from the slope. The dielectric capacitance C_d in the equivalent circuit of a DBD does not depend on the external applied voltage's amplitude, since this capacitance is determined by the fixed geometry of the DBD system.⁴ All Q-V plots obtained with different amplitudes of the applied voltage

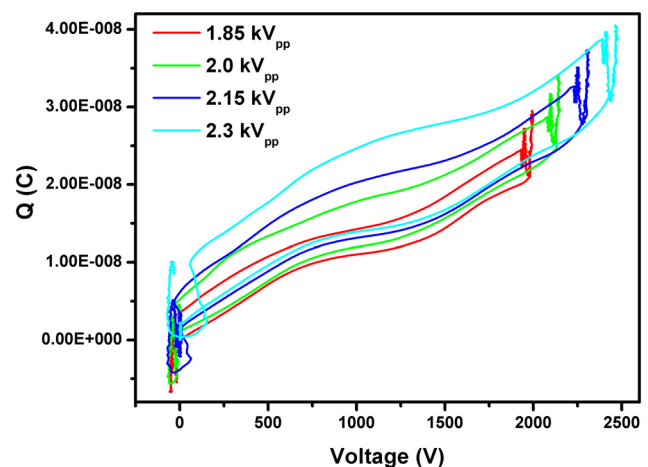


FIG. 2. Q-V plots for different amplitudes of the applied voltage. Here, Q was obtained using Eq. (2), namely, through the integration of the discharge current.

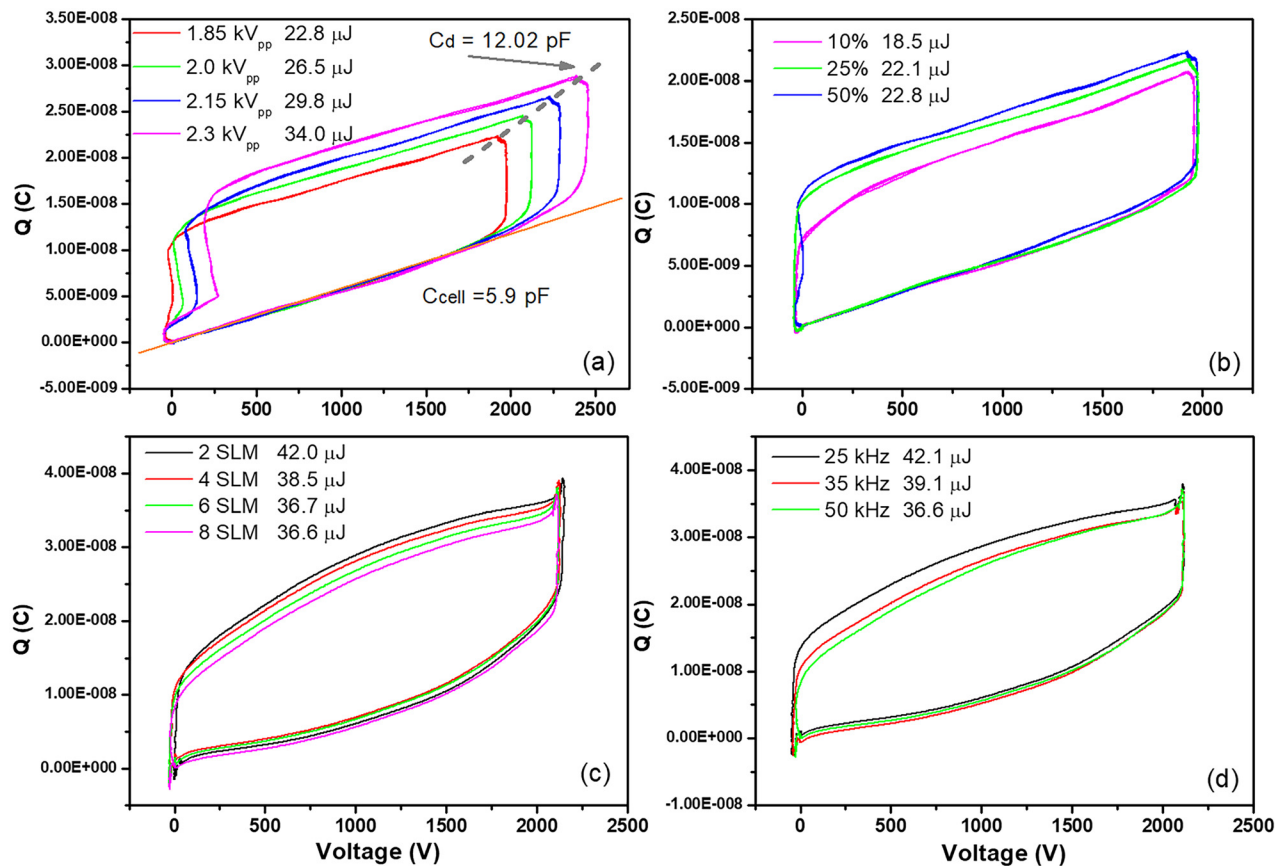


FIG. 3. (a) Q-V plots for different amplitudes of the applied voltage (3 SLM, 50 kHz, and 50%). Here, Q was obtained using an additional capacitance connected to the ground. The dotted and straight solid lines represent the determined values of C_d and C_{cell} , respectively. Q-V plots for (b) different duty ratios (3 SLM, 50 kHz, and 1.85 kV_{pp}), (c) different gas flow rates (50 kHz, 2.15 kV_{pp}, and 50%), and (d) different pulse frequencies (8 SLM, 2.15 kV_{pp}, and 50%) are also shown. The figures contain the converted electrical energy per pulse, E , which was calculated as the enclosed area in the Q-V plot.

are shown in Fig. 3(a).²⁰ The upper corner of the Q-V plot represents Q_{max} at given V_{max} . It is recommended that the capacitance of dielectric barriers be obtained from a plot of the maximal charge vs maximal voltage amplitude ($Q_{max}-V_{max}$ plot) in a manner analogous to the classical approach. At some voltage amplitude, the charge is transferred without a significant increase in the applied voltage, and the charge transfer is related to a drop in the applied voltage caused by the breakdown (the discharge ignition and to the rapid change in the effective reactor capacitance).¹⁹

Figure 3(a) shows that the estimated values of C_d and C_{cell} were 12.02 and 5.9 pF, respectively. The enclosed area (E) of the Q-V Lissajous figure provides the electrical energy per cycle. The calculated E values are tabulated for each experimental condition in Figs. 3(a)–3(d); the transferred electrical energy (E) increases with increasing amplitude of the applied voltage. It is about 34.04 μ J for $U_a = 2.3$ kV and decreases to approximately 22.86 μ J for $U_a = 1.85$ kV. The dissipated power P_{diss} can also be easily calculated by multiplying E by the pulse frequency f . For the pulse frequency of 50 kHz, the power can be calculated to be about 1.7 W ($U_a = 2.3$ kV) and 1.14 W ($U_a = 1.85$ kV), respectively. As shown in Fig. 3(a), for the voltage amplitudes of 1.85, 2.0, 2.15, and 2.3 kV, the applied voltage at the time of breakdown, U_{min} ($U_{min} \approx 1.82$ kV), did not

change. This indicates that the minimum external voltage at which the ignition occurs does not depend on the applied voltage, which implies that residual charges deposited on dielectric barriers during previous ignition do not play a significant role in this experimental condition of low applied voltages.

Figure 3(b) shows Q-V plots for different duty ratios. As discussed in our previous paper,¹¹ the electrical energy per cycle, E , increased with the duty ratio. Figure 3(c) shows Q-V plots for different gas flow rates (2.0, 4.0, 6.0, and 8.0 SLM). Note that E decreased with an increase in the gas flow rate. Increasing the gas flow rate (which would decrease the electron temperature) decreases the streamer velocity (i.e., the ionization wave front velocity) and hence the discharge current. Therefore, the electrical energy decreased with an increasing gas flow rate.

In Fig. 3(d), Q-V plots are shown as a function of the pulse frequency, where E decreases with an increase in the pulse frequency. Figures 3(a)–3(d) contain the converted electrical energy per pulse, which was calculated as the enclosed area of the Q-V plot.

From Eqs. (2)–(4), the temporal evolution of U_g , I_R , and P_g was determined from measured waveforms of $U_a(t)$, $Q(t)$, and the discharge current [instead of $I_t(t)$] at fixed conditions ($U_a = 2.3$ kV and

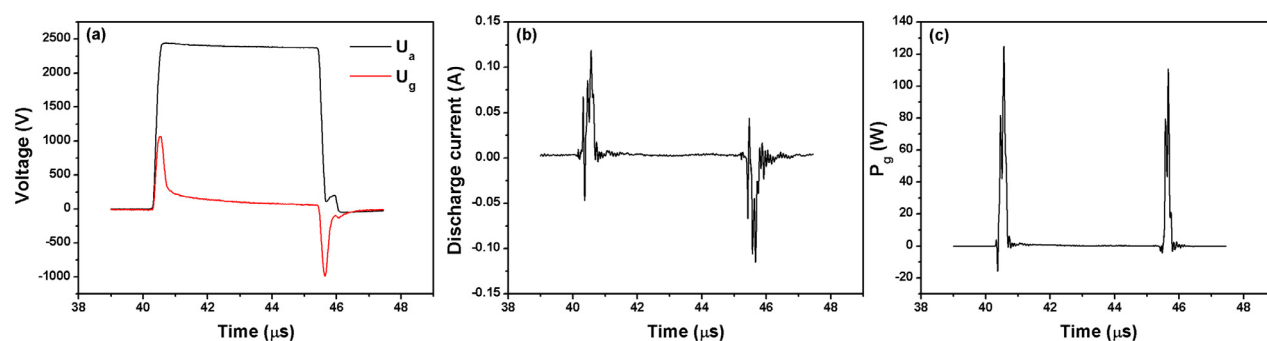


FIG. 4. Temporal profiles of the (a) measured applied voltage and calculated gap voltage, (b) corresponding discharge current, and (c) calculated instantaneous power. The applied voltage was 2.3 kV_{pp}, and the duty ratio was 25%.

duty ratio = 25%). The results are shown in Figs. 4(a)–4(c). The electrical energy that is dissipated into the plasma in each cycle of the voltage pulses can also be obtained as $E = \int_0^T P_g(\tau) d\tau$. The enclosed area in the Q - V plot provides the value of 32.29 μJ , while the integration of P_g yielded 31.34 μJ . The difference between both estimates is not significant. It is noteworthy that considering the level of applied voltage amplitude, the unipolar square pulse is more efficient than a bipolar pulse in terms of the electrical energy produced per pulse.¹³

In the case of the DBD-based plasma jet employed in this study, as long as the flow was laminar, the plasma plume length increased with the gas flow rate, as shown in Fig. 5(a).²² Usually, an increase in gas feeding results in jet elongation, and a further increase of up to 8 SLM in the flow rate causes jet shortening and the appearance of a turbulent tail.²³ For laminar flow, with an increase in the gas flow rate, the distance from the nozzle to the position where there is noticeable mixing of the working gas inside the gas stream with the surrounding air also increases, which results in a larger streamer propagation length.²² On the other hand, the effect of the pulse frequency on the plasma plume length is not monotonous. When the pulse frequency increases at a fixed duty ratio, the pulse width decreases, and the decay time between successive streamers is reduced; the concentrations of reactive species increase immediately before the start of the next streamer, which affects the subsequent discharge.²² In a work performed by Xiong *et al.*,²⁴ when the pulse frequency was varied from 0.1 to 10 kHz, the length of the plasma plume did not change significantly. However, in this study, where a discharge occurred along the coaxial DBD electrode, when the pulse frequency was increased from 20 to 50 kHz, the plasma plume length decreased slightly, which could be attributed to the effect of the pulse width.^{25–27} Since the duty ratio was fixed at 8%, the pulse widths for 20, 35, and 50 kHz were 4.0, 2.28, and 1.6 μs , respectively. In this study, when short-pulse widths were employed, the ionization front was prematurely terminated by the falling edge of the applied voltage pulse. Consequently, the energy dissipation became small, resulting in weak discharges. This also explains that E decreases with an increase in the pulse frequency in Fig. 3(d).

Figure 5(b) shows the optical emission spectrum of the jet. The strongest emission bands, the N_2^+ second positive system at 337 nm and the N_2^+ first negative system at 391 nm, are associated with molecular nitrogen and ionic molecular nitrogen. The hydroxyl (OH) radical (peak at 309 nm) is produced via dissociative electron attachment with water vapor molecules. Since the OH radical can induce an

important biological function, the observed high intensity of OH would be advantageous for liquid treatments.²⁸ The 706 nm emission of He indicates the presence of energetic energy electrons with energies above 20.96 eV, and this line can be considered as a reference transition for He discharges. The 777 nm line originates from highly reactive excited O atoms. The characteristic spectral lines of helium at 587, 667, 706, and 728 nm were selected to determine the excitation temperature (T_{exc}) by using the Boltzmann approximation. The inset of Fig. 5(b) shows the excitation temperature as a function of the gas flow rate and pulse frequency. It can be observed that T_{exc} slightly decreases with an increase in the gas flow rate and pulse frequency. The frequency effect appears to be related to the pulse width, as mentioned earlier.

The collisional radiative model of Gangwar *et al.* predicts line ratios from triplet states 587 nm (He: $3d^3D \rightarrow 2p^3P$) to 706 nm (O: $3s^3S \rightarrow 2p^3P$) and singlet states 667.8 nm (He: $3d^1D \rightarrow 2p^1P$) to 728.1 nm (He: $3d^1S \rightarrow 2p^1P$), which depend only on the electron temperature.²⁹ Figure 5(c) shows the emission intensity ratios of He (587 nm) to He (706 nm) and He (667 nm) to He (728 nm) as functions of the gas flow rate and pulse frequency. The variations in these line ratios are similar to those of the excitation temperature, which is proportional to the electron energy. Figure 5(d) also shows that the species density increases with the frequency. Figures 5(e) and 5(f) show the gas temperature and ozone concentration in the gas phase as functions of the gas flow rate at different pulse frequencies, respectively. The gas temperature and ozone concentration slightly increased with an increase in the pulse frequency. As will be discussed later on, for higher pulse frequency, the second ionization front is subjected to a stronger local electric field at the instant of its ignition. This could explain the important increase in the mean velocity of ionization front, the slight increase in gas temperature, and the slight increase in the ozone concentration.⁷ By contrast, both these parameters decreased slightly with an increase in the gas flow rate. This can be explained by the fact that increasing the gas flow rate (which would decrease the electron temperature) decreases the streamer velocity (i.e., the ionization wave front velocity) and hence the discharge current. Since the gas temperature correlates with the electron temperature (and ozone concentration is dependent on gas temperature), they decrease with an increasing gas flow rate.

Figures 6(a) and 6(b) show the dependence of the discharge current on the gas flow rate and pulse frequency, respectively. Clearly, a discharge current was generated during the rising and falling edges of

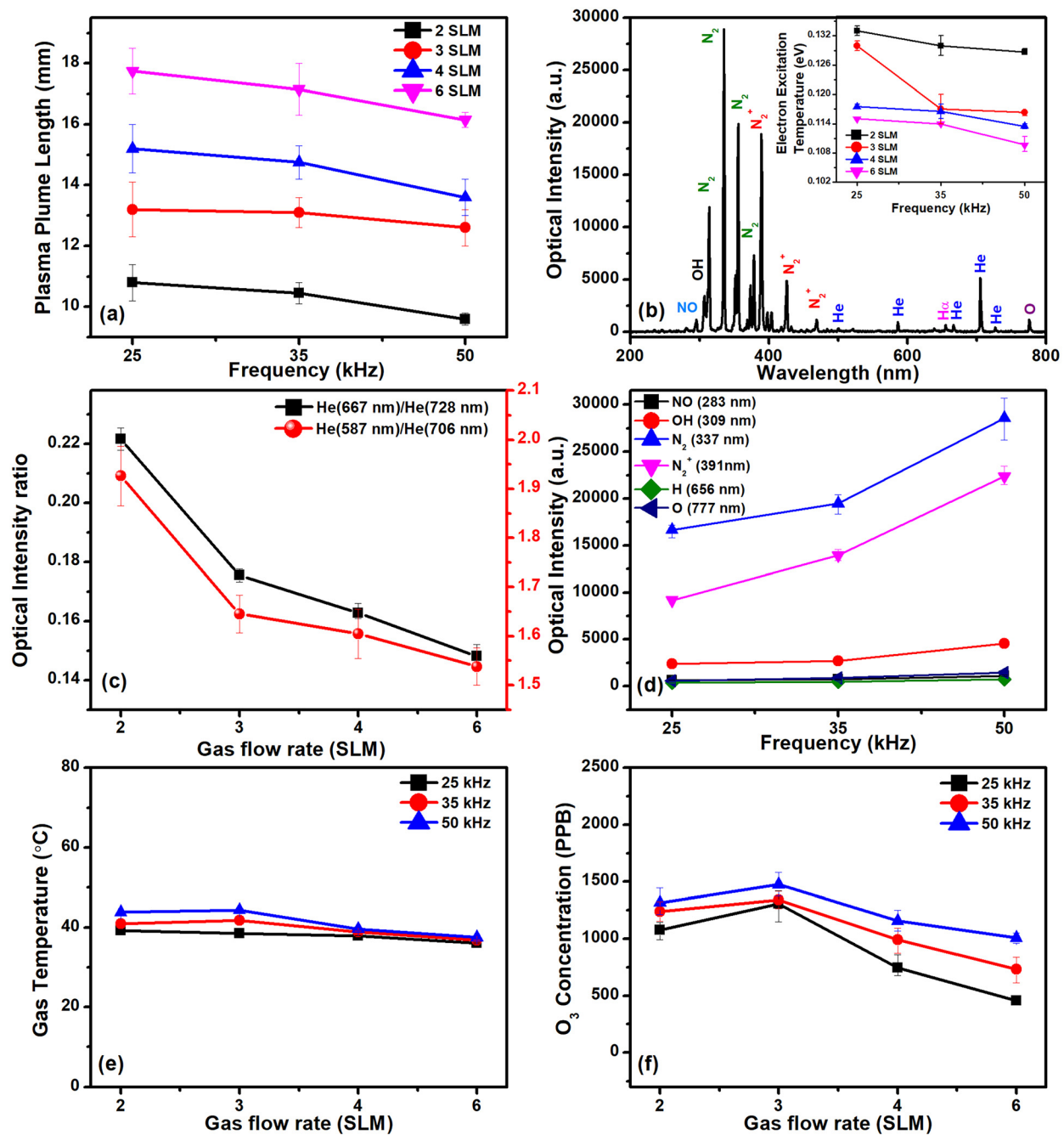


FIG. 5. (a) Plume length as functions of the gas flow rate and pulse frequency (1.9 kV_{pp}, 8%). (b) A typical optical emission spectrum of the jet plasma (3 SLM, 50 kHz, 2.3 kV_{pp}, 5%). The inset shows the excitation temperature estimated using the Boltzmann plot as functions of the gas flow rate and pulse frequency (2.3 kV_{pp}, 5%). (c) Intensity ratios of two atomic lines: He (587 nm)/He (706 nm) and He (667 nm) to He (728 nm) (50 kHz, 2.3 kV_{pp}, 5%). (d) Emission intensities as a function of the pulse frequency (4 SLM, 2.3 kV_{pp}, 5%). (e) Gas temperature and (f) ozone concentration in the gas phase plotted as functions of the gas flow rate at different pulse frequencies. For (a)–(c), the applied voltage was 2.0 kV.

the applied voltage pulse, namely, the primary and secondary discharge, respectively. The discharge current amplitude at both primary and secondary discharges decreased slightly with an increase in the gas flow rate. This may be attributed to the ionization wave front velocity

due to electron diffusion, which depends on the ionization frequency and ambipolar diffusion coefficient.^{23,30} Both ionization frequency and ambipolar diffusion coefficient are dependent on the electron temperature, and therefore, increasing the gas flow rate (which would decrease

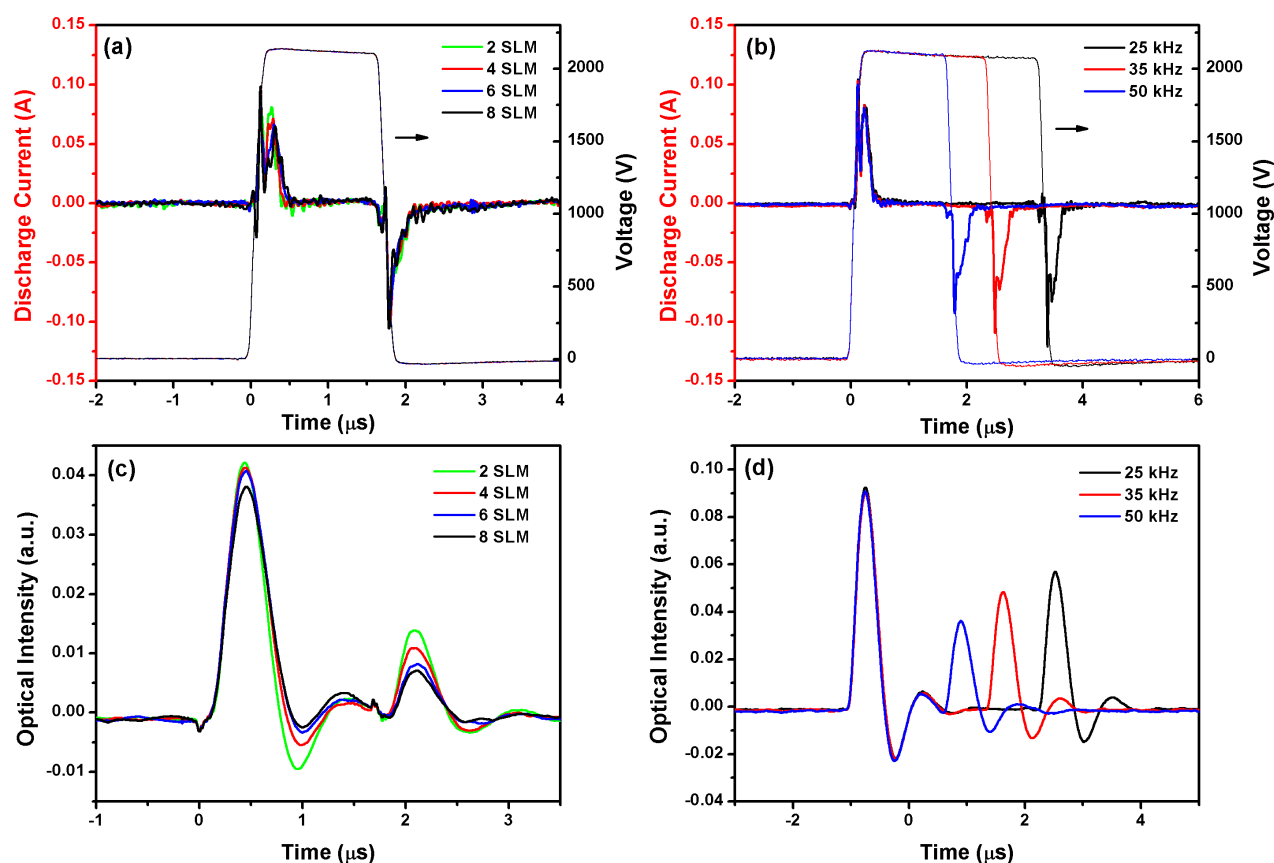


FIG. 6. Typical oscillogram of the driving pulsed voltage, discharge current, and ionization front light emission for [(a) and (b)] different gas flow rates (50 kHz, 2.0 kV_{pp}, 8%) and [(c) and (d)] pulse frequencies (2 SLM, 2.0 kV_{pp}, 8%). The light emission was wavelength-integrated over the 300–1000 nm range, and the probed zone was along 5 mm downstream of the reactor tube's orifice.

the electron temperature) decreases the streamer velocity (i.e., the ionization wave front velocity) and hence the discharge current. Furthermore, the discharge current at the secondary discharge increased with the pulse frequency. As the pulse frequency increased (i.e., the pulse width decreased), although the cathode-directed streamer velocity remained almost constant, the second front velocity increased significantly.⁷

Figures 6(c) and 6(d) show the temporal evolution of the wavelength-integrated emission intensity as a function of the gas flow rate and pulse frequency, respectively. Two discrete ionization fronts were apparently generated. The first was due to the primary discharge, being related to a cathode-directed streamer propagating into the helium channel,⁷ and the second front was associated with the secondary discharge, being caused by the residual ionic space charge formed in the wake of the cathode-directed streamer propagation. As the gas flow rate increased from 2 to 8 SLM, the second front weakened, and as the pulse frequency increased, the second front became stronger. Overall, the discharge current correlated well with light emission.

As mentioned before, in secondary discharge (that is, during a negative gap voltage), the two electric fields (the local electric field and the externally applied electric field) are in the opposite direction, and so the effective electric field is reversed, which results in the negative currents [see Figs. 6(a) and 6(b)]. The current depends on the strength

of the effective electric field, which is influenced by the operational parameters such as gas flow rate and pulse frequency (or pulse width). It is observed that the magnitude of current correlates with the intensity of light emission [see Figs. 6(c) and 6(d)]. For long enough pulse widths (or lower pulse frequency at a fixed duty ratio), the second ionization front is subjected to a weaker local electric field at the instant of its ignition since the residual charge has previously drifted apart.^{7,11,12,26} Therefore, the second ionization front appears weaker and slower. This could explain the important decrease in the mean velocity and the slight decrease in the chemical reactivity.⁷

B. APPJ treatment of various media

It has been reported that plasma-activated media can be useful in eradicating various cancer cell lines.³¹ Because the use of APPJs for cancer cell treatment has been shown to be effective,^{1,12} here, we simply report on measurements of concentrations of hydrogen peroxide and nitrite, species known to be important biological effectors, produced when DW or essential culture media are exposed to APPJs.

A large number of RONS are produced in a plasma-treated liquid, and the physical and chemical properties of the liquid, including the pH and electrical conductivity, change significantly; the pH and

electrical conductivity are important factors in biomedical applications, such as bacterial inactivation.³² The biochemical activity of plasma-activated media (PAM) results from the synergistic effects of the highly reactive species, particularly the RONS.³³

Different media [DW, serum-free Hanks' balanced salt solution (HBSS), Roswell Park Memorial Institute (RPMI), phosphate buffered saline (PBS), and Dulbecco's modified Eagle medium (DMEM)] were subjected to APPJ treatment, and changes in the RONS concentration were examined as a function of the operational parameters and storage conditions. It is believed that the overall post-discharge bactericidal and/or cytotoxic effect of the plasma-liquid system involves the synergistic effect of acidic conditions, nitrites, and peroxides through the cytotoxic activity of secondary reactive chemical species NO, NO₂, OH, and ONOOH, and possibly also contribution of ozone transferred from the plasma into the liquid.²⁸

To quantify the concentration of stable RONS in the plasma-treated media, the H₂O₂ concentration was measured using UV-visible spectrophotometry for different treatment conditions. For the determination of the NO₂⁻ concentration, the standard procedure of the Griess assay was followed. As shown in Figs. 7(a)–7(f) [H₂O₂] and [NO₂⁻] were determined after the plasma treatment of 3 ml of media.

[H₂O₂] and [NO₂⁻] in the PAM were detected at 0, 1, 2 h, and 7 days after the plasma exposure. The PAM were stored in the refrigerator with temperature control in the darkness. The RONS concentration was dependent on the media type, and it increased in the order of HBSS, DMEM, PBS, and DW. The levels of [H₂O₂] and [NO₂⁻] in the PAM increased with both the plasma exposure time and gas flow rate [Figs. 7(a) and 7(b)]. [H₂O₂] and [NO₂⁻] in the PAM were also observed to increase with the pulse frequency [Figs. 7(c) and 7(d)]. This could be explained by the fact that as the pulse frequency increased, the decay time between successive streamers decreased, and hence, the concentrations of reactive species increased immediately before the start of the next streamer. It is noteworthy that the DBD-based pulsed APPJ with a low/moderate voltage (power: 1.5 W) could provide a production level of RONS ([H₂O₂] and [NO₂⁻]) that was almost comparable to that achieved with an APPJ array (composed of 16 multiple jets; power: 5 W)²⁷ or a microwave-driven (2.45 GHz) Ar plasma jet (power: 5–8 W).³⁴ This strongly indicates the high efficiency of a pulsed DBD-based jet in the treatment of cell culture media. An assessment of the time evolution of the PAM indicated that the RONS concentration in the PAM was stable up to 2 h (not shown in the figure). PAM has proven to remain stable after a relatively long storage time (hours to days depending on the storage temperature). Generally, the RONS concentration was better maintained when the PAM were stored at 4 °C compared with those stored at room temperature and at –20 °C [Figs. 7(e) and 7(f)]. This long-term stability suggests that through an appropriate choice of the treatment and storage conditions, PAM with a farther expiration date can be obtained.³⁵

Figure 8 shows the pH level and electrical conductivity of the plasma-treated DW. The decreased pH value suggests a high concentration of RONS in the treated DW, which could explain the increase in the electrical conductivity after the APPJ treatment. The observed changes in the pH and electrical conductivity can be attributed to the concentrations of N₂^{*}, O, H, and OH radicals, which were generated in the plasma and plasma-liquid transition region. These radicals were

generated because of plasma expansion in ambient air as well as the vaporization and dissociation of water molecules.³⁵ Evidently, as the pulse frequency increased, the chemical reactivity increased, as mentioned before,⁷ resulting in a decrease in the pH and an increase in the electrical conductivity [Figs. 8(a) and 8(b)]. As apparent in Figs. 8(c) and 8(d), an increase in the gas flow rate resulted in a slightly lower pH level and a higher electrical conductivity in the DW. Oehmigen *et al.* reported that the formation of H⁺ and HNO₃⁻ is mainly responsible for the acidification of plasma-treated water.³⁶ Ikawa *et al.* proposed that both NO₂⁻ and NO₃⁻ contribute to the pH drop.³² However, Vlad *et al.* suggested that the increase in the acidification and electrical conductivity of plasma-treated water was because of the formation of NO₃⁻/HNO₃, identical to a nitric acid solution.³⁵ It is also noteworthy that the pH level and electrical conductivity did not change much even after one week's storage, and 24 °C was the best choice of storage temperature [Figs. 8(e) and 8(f)]. As shown in Fig. 8(g), the ozone concentration in the APPJ-treated DW increased with both the gas flow rate and pulse frequency. It is generally believed that after being produced in a gas phase, ozone can be transported across an interface into a liquid.³³ However, a comparison of Fig. 8(g) with the ozone concentration in the gas phase [Fig. 5(f)] indicates that the ozone concentration varies differently with the gas flow rate and pulse frequency in gas and liquid phases. This implies that ozone can be generated or destroyed directly in solution via various reactions with other RONS.³⁷

Although the electrical energy calculated using Q-V plots indicated that *E* decreased with an increase in the gas flow rate and pulse frequency, the RONS concentration and physicochemical properties exhibited the opposite behavior. This discrepancy can be explained in two aspects. The first one to consider is that the results of 2D simulation performed by Schweigert *et al.* showed that the plasma density between nozzle and target, produced by the streamers of previous voltage pulses and decreased by the recombination, can be large enough to stop the streamer propagation or let it go through the plasma cloud for different repetitive modes.³⁸ In other words, not every streamer generated by the voltage pulse will successfully reach the target surface. This self-organization determines the energy input near the target and consequently the electromagnetic and chemical interaction of plasma with the target.³⁸ The second one is associated with the transport of RONS into the plasma-liquid interface. It is generally inferred that instantaneous evolution of power and associated optical transitions contribute to the formation of reactive species in the gas phase. If the pulse width is fixed, the pulse frequency is directly related to the power supplied to the system. For normal power supply, the pulse frequency also governs the pulse width, which influences the internal dynamics of the discharge. Generally, a power increase leads to higher energy being deposited onto physicochemical reactions.⁷ However, it should be noted that a plasma plume delivers reactive species to a liquid's surface, where many important physicochemical reactions start to occur at the plasma-liquid interface and in the bulk liquid. The energy dissipated in the plasma (i.e., electrical energy) is not the only factor that determines the generation of reactive species in a treated solution. Therefore, the correlation of plasma-generated long-lived reactive species in aqueous and gas phases should be investigated from a broader perspective.^{38,39}

V. CONCLUSION

A coaxial DBD-based APPJ in helium driven by square voltage pulses was characterized. Furthermore, by combining a simplified equivalent circuit model with a transferred charge (*Q*) measured by

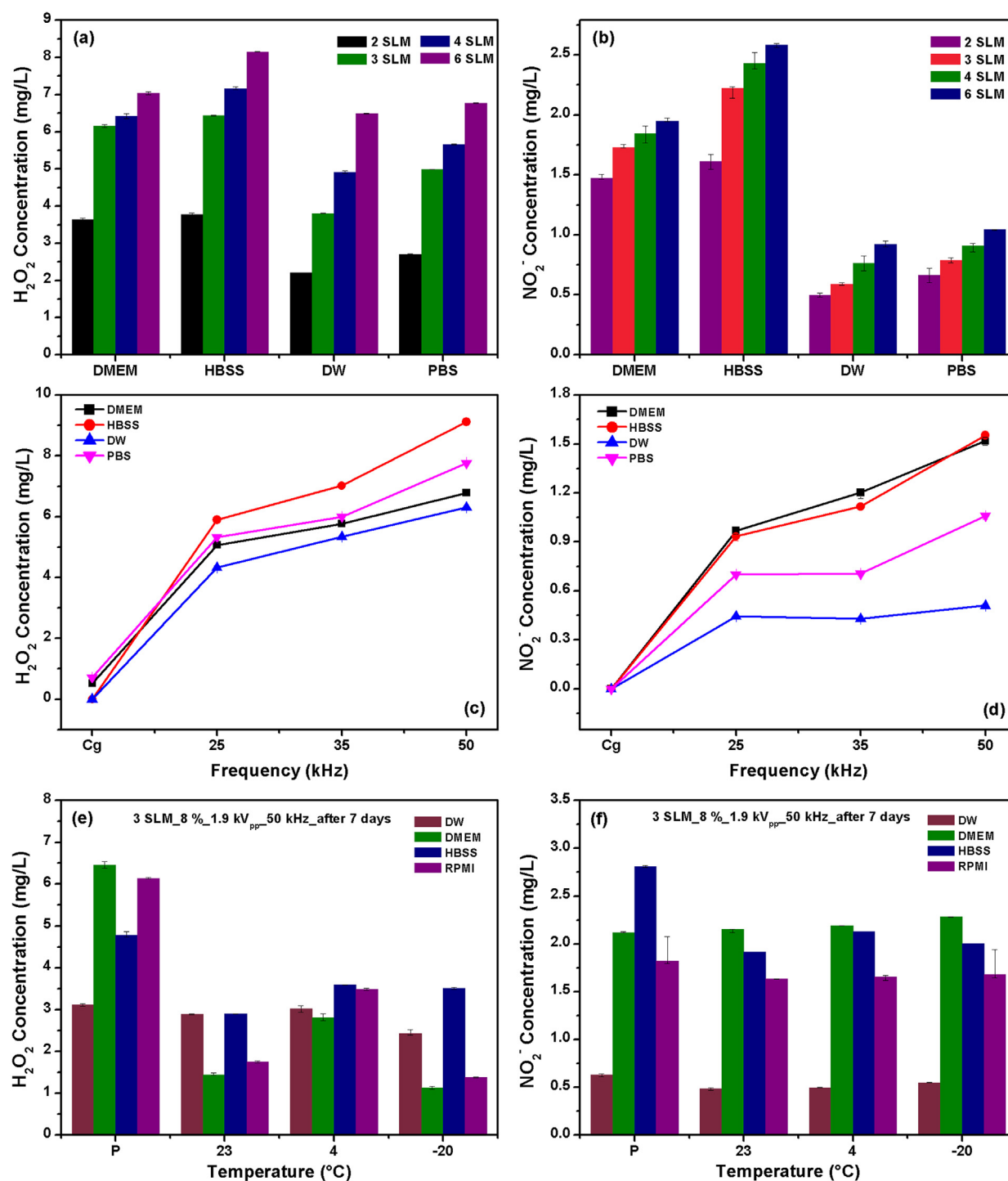


FIG. 7. Quantification of the stable RONS in plasma-treated DW. (a) $[\text{H}_2\text{O}_2]$ and (b) $[\text{NO}_2^-]$ in different media (DMEM, HBSS, PBS, and DW) immediately after the plasma treatment as a function of the gas flow rate (50 kHz, 1.9 kV_{pp}, 8%). (c) $[\text{H}_2\text{O}_2]$ in different media as a function of the pulse frequency (3 SLM, 1.9 kV_{pp}, 8%). (d) $[\text{NO}_2^-]$ in different media as a function of the pulse frequency (4 SLM, 1.9 kV_{pp}, 8%). (e) $[\text{H}_2\text{O}_2]$ in different media (DMEM, HBSS, PBS, and DW) under different storage conditions seven days after the plasma treatment. P denotes media immediately after the plasma treatment. (f) $[\text{NO}_2^-]$ in different media (DMEM, HBSS, PBS, and DW) under different storage conditions seven days after the plasma treatment (3 SLM, 50 kHz, 1.9 kV_{pp}, 8%). In all cases, the volume of DW was 3 ml, the treatment time was 3 min, and the nozzle-to-liquid distance was 12 mm.

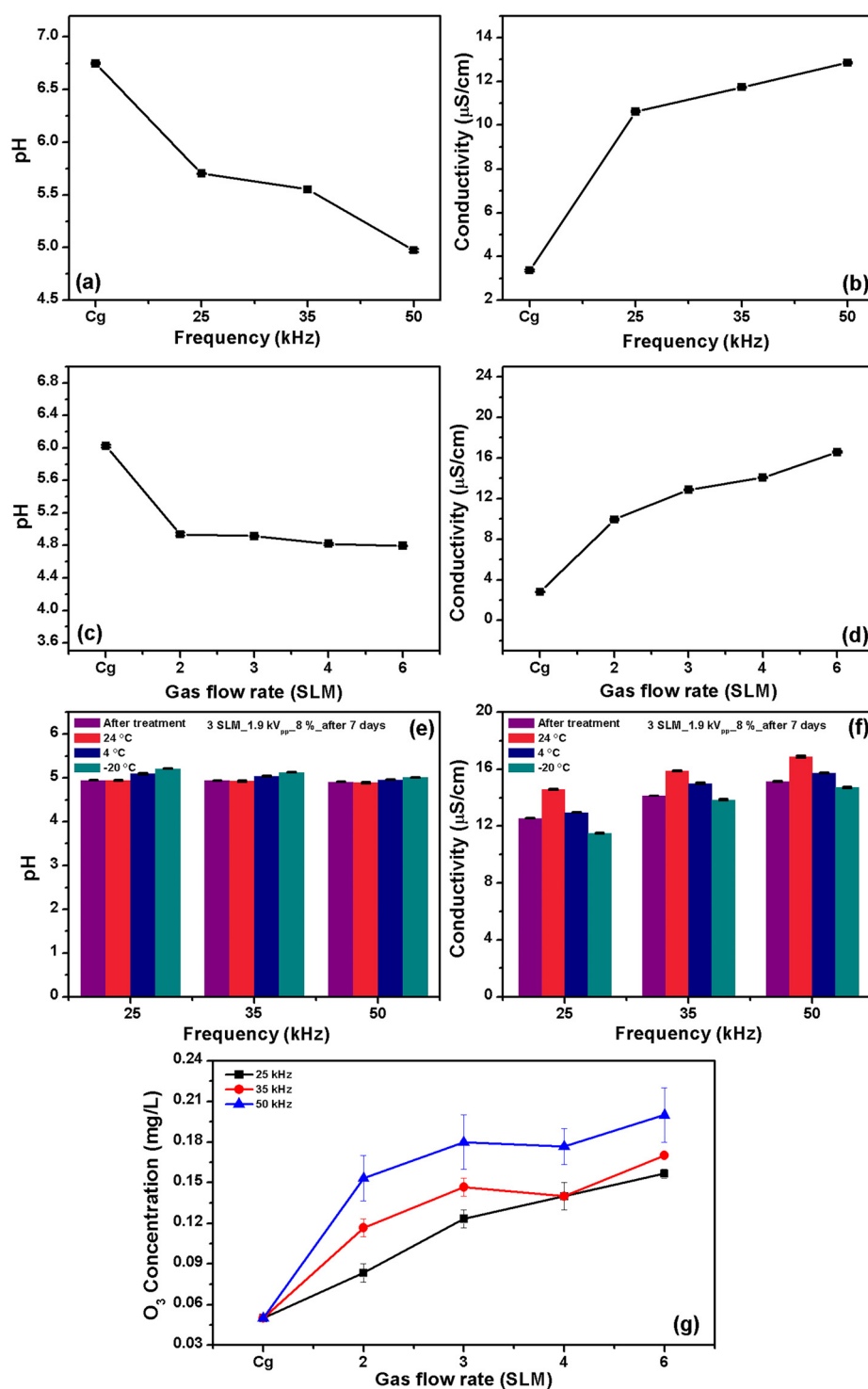


FIG. 8. (a) The pH and (b) electrical conductivity of the plasma-treated DW as functions of the pulse frequency (3 SLM, 1.9 kV_{pp}, 8%). (c) The pH and (d) electrical conductivity of the plasma-treated DW as functions of the gas flow rate (50 kHz, 1.9 kV_{pp}, 8%). (e) and (f) The pH and electrical conductivity after seven days at a storage temperature of 4 °C (3 SLM, 1.9 kV_{pp}, 8%). C_g denotes gas control. (g) Ozone concentration in the APPJ-treated DW as functions of the gas flow rate and pulse frequency (1.9 kV_{pp}, 8%). In all cases, the volume of DW was 3 ml, the treatment time was 3 min, and the nozzle-to-liquid distance was 12 mm.

introducing an additional capacitance in series with the reactor, a miniature pulse-voltage-driven DBD was characterized. From Q-V plots, C_d and C_{cell} for DBD reactors under pulsed excitation were determined. The method is based on the consideration of Q-V plots

measured at several voltage amplitudes. Q-V plots were drawn for varying operational parameters, and the dissipated energy per cycle was evaluated. As an application, cell culture media, including DW, were exposed to an APPJ, and their properties (pH and electrical

conductivity) and concentrations of reactive species generated in them were measured as functions of the operational parameters. For the cell culture media, it was noted that a DBD-based pulsed APPJ with a low/ or moderate voltage (power: 1.5 W) achieved a RONS production level that was almost comparable to that obtained with an APPJ array (composed of 16 multiple jets; power: 5 W) or a microwave-driven (2.45 GHz) Ar plasma jet (power: 5–8 W). Furthermore, the physico-chemical properties of PAM were found to remain stable over a week for different storage times and conditions. This showed the high efficiency of the pulsed DBD-based jet in the treatment of cell culture media. The correlation between plasma characteristics and reactive species generation is discussed. It should be noted that reactive species generation in target liquids depends not only on the energy dissipated in the plasma phase but also on the transport of reactive species along the gas channel to the target liquid.

ACKNOWLEDGMENTS

This work was supported by the National Research Foundation of Korea under Contract No. 2022R1A2C1006170.

AUTHOR DECLARATIONS

Conflict of Interest

The authors have no conflicts to disclose.

Author Contributions

Min Jeong Seong: Data curation (equal); Formal analysis (equal). **Yun Jeong Ha:** Investigation (equal). **Gun Hyeon Park:** Investigation (equal). **Sun Ja Kim:** Data curation (equal); Investigation (equal). **Hea Min Joh:** Project administration (equal). **Tae Hun Chung:** Conceptualization (equal); Writing – original draft (equal).

DATA AVAILABILITY

The data that support the findings of this study are available from the corresponding author upon reasonable request.

REFERENCES

- S. J. Kim and T. H. Chung, "Cold atmospheric plasma jet-generated RONS and their selective effects on normal and carcinoma cells," *Sci. Rep.* **6**, 20332 (2016).
- U. Kogelschatz, "Dielectric-barrier discharges: Their history, discharge physics, and industrial applications," *Plasma Chem. Plasma Process.* **23**, 1–46 (2003).
- H.-E. Wagner, R. Brandenburg, K. V. Kozlov, A. Sonnenfeld, P. Michel, and J. F. Behnke, "The barrier discharge: Basic properties and applications to surface treatment," *Vacuum* **71**, 417 (2003).
- F. J. J. Peeters and M. C. M. van de Sanden, "The influence of partial surface discharging on the electrical characterization of DBDs," *Plasma Sources Sci. Technol.* **24**, 015016 (2015).
- M. Kettlitz, H. Hoft, T. Hoder, S. Reuter, K.-D. Weltmann, and R. Brandenburg, "On the spatio-temporal development of pulsed barrier discharges: Influence of duty cycle variation," *J. Phys. D* **45**, 245201 (2012).
- X. Lu, D. W. Liu, Y. Xian, L. L. Nie, Y. G. Cao, and G. Y. He, "Cold atmospheric-pressure air plasma jet: Physics and opportunities," *Phys. Plasmas* **28**, 100501 (2021).
- K. Gazeli, P. Svarnas, C. Lazarou, C. Anastassiou, G. E. Georgiou, P. K. Papadopoulos, and F. Clement, "Physical interpretation of a pulsed atmospheric pressure plasma jet following parametric study of the UV-to-NIR emission," *Phys. Plasmas* **27**, 123503 (2020).
- M. Laroussi and T. Akan, "Arc-free atmospheric pressure cold plasma jets: A review," *Plasma Process. Polym.* **4**, 777 (2007).
- J. L. Walsh, J. J. Shi, and M. G. Kong, "Contrasting characteristics of pulsed and sinusoidal cold atmospheric plasma jets," *Appl. Phys. Lett.* **88**, 171501 (2006).
- P. Reichen, A. Sonnenfeld, and P. Rudolf von Rohr, "Discharge expansion in barrier discharge arrangements at low applied voltages," *Plasma Sources Sci. Technol.* **20**, 055015 (2011).
- J. H. Bae, J. J. Mun, M. J. Seong, S. J. Kim, H. M. Joh, and T. H. Chung, "Effects of duty ratio on liquid- and polymer-surface treatment by a unipolar microsecond-pulsed helium atmospheric-pressure plasma jet," *Phys. Plasmas* **30**, 043515 (2023).
- S. J. Kim and T. H. Chung, "Plasma effects on the generation of reactive oxygen and nitrogen species in cancer cells in-vitro exposed by atmospheric pressure pulsed plasma jets," *Appl. Phys. Lett.* **107**, 063702 (2015).
- D. Y. Kim, S. J. Kim, H. M. Joh, and T. H. Chung, "Characterization of an atmospheric pressure plasma jet array and its application to cancer cell treatment using plasma activated medium," *Phys. Plasmas* **25**, 073505 (2018).
- A. Khlyustova, C. Labay, Z. Machala, M.-P. Ginebra, and C. Canal, "Important parameters in plasma jets for the production of RONS in liquids for plasma medicine: A brief review," *Front. Chem. Sci. Eng.* **13**, 238 (2019).
- K. Kim, H. J. Ahn, J.-H. Lee, J.-H. Kim, S. S. Yang, and J. H. Lee, "Cellular membrane collapse by atmospheric-pressure plasma jet," *Appl. Phys. Lett.* **104**, 013701 (2014).
- S. Liu and M. Neiger, "Electrical modelling of homogeneous dielectric barrier discharges under an arbitrary excitation voltage," *J. Phys. D* **36**, 3144 (2003).
- S. Tao, L. Kaihua, Z. Cheng, Y. Ping, Z. Shichang, and P. Ruzheng, "Experimental study on repetitive unipolar nanosecond-pulse dielectric barrier discharge in air at atmospheric pressure," *J. Phys. D* **41**, 215203 (2008).
- F. Massines, A. Rabehi, P. Decomps, R. Gadri, P. Ségur, and C. Mayoux, "Experimental and theoretical study of a glow discharge at atmospheric pressure controlled by dielectric barrier," *J. Appl. Phys.* **83**, 2950 (1998).
- A. V. Pipa, T. Hoder, J. Koskulics, M. Schmidt, and R. Brandenburg, "Experimental determination of dielectric barrier discharge capacitance," *Rev. Sci. Instrum.* **83**, 075111 (2012).
- A. V. Pipa, J. Koskulics, R. Brandenburg, and T. Hoder, "The simplest equivalent circuit of a pulsed dielectric barrier discharge and the determination of the gas gap charge transfer," *Rev. Sci. Instrum.* **83**, 115112 (2012).
- J.-S. Boisvert, L. Stafford, N. Naudé, J. Margot, and F. Massines, "Electron density and temperature in an atmospheric-pressure helium diffuse dielectric barrier discharge from kHz to MHz," *Plasma Sources Sci. Technol.* **27**, 035005 (2018).
- X. Lu, G. V. Naidis, M. Laroussi, and K. Ostrikov, "Guided ionization waves: Theory and experiments," *Phys. Rep.* **540**, 123 (2014).
- H. S. Park, S. J. Kim, H. M. Joh, T. H. Chung, S. H. Bae, and S. H. Leem, "Optical and electrical characterization of an atmospheric pressure micro-plasma jet with a capillary electrode," *Phys. Plasmas* **17**, 033502 (2010).
- Q. Xiong, X. Lu, K. Ostrikov, Z. Xiong, Y. Xian, F. Zhou, C. Zou, J. Hu, W. Gong, and Z. Jiang, "Length control of He atmospheric plasma jet plumes: Effects of discharge parameters and ambient air," *Phys. Plasmas* **16**, 043505 (2009).
- Z. J. Liu, C. X. Zhou, D. X. Liu, D. H. Xu, W. J. Xia, Q. J. Cui, B. C. Wang, and M. G. Kong, "Production and correlation of reactive oxygen and nitrogen species in gas- and liquid-phase generated by helium plasma jets under different pulse widths," *Phys. Plasmas* **25**, 013528 (2018).
- H. M. Joh, E. J. Baek, S. J. Kim, and T. H. Chung, "Effects of the pulse width and oxygen admixture on the production of reactive species in gas- and liquid-phases exposed by bipolar microsecond-pulsed atmospheric pressure helium plasma jets," *Phys. Plasmas* **26**, 053509 (2019).
- A. Jo, H. M. Joh, J. H. Bae, S. J. Kim, T. H. Chung, and J. W. Chung, "Plasma activated medium prepared by a bipolar microsecond-pulsed atmospheric pressure plasma jet array induces mitochondria-mediated apoptosis in human cervical cancer cells," *PLoS One* **17**(8), e0272805 (2022).
- P. Lukes, E. Dolezalova, I. Sisrova, and M. Clupek, "Aqueous-phase chemistry and bactericidal effects from an air discharge plasma in contact with water: Evidence for the formation of peroxyxynitrite through a pseudo-second-order

- post-discharge reaction of H_2O_2 and HNO_2 ,” *Plasma Sources Sci. Technol.* **23**, 015019 (2014).
- ²⁹R. K. Gangwar, O. Levasseur, N. Naudé, N. Gherardi, F. Massines, J. Margot, and L. Stafford, “Determination of the electron temperature in plane-to-plane He dielectric barrier discharges at atmospheric pressure,” *Plasma Sources Sci. Technol.* **25**, 015011 (2016).
- ³⁰A. Böhle, O. Ivanov, A. Kolisko, U. Kortshagen, H. Schlüter, and A. Vikharev, “Pulsed discharges produced by high-power surface waves,” *J. Phys. D* **29**, 369 (1996).
- ³¹S. Mohades, M. Laroussi, J. Sears, N. Barekzi, and H. Razavi, “Evaluation of the effects of a plasma activated medium on cancer cells,” *Phys. Plasmas* **22**, 122001 (2015).
- ³²S. Ikawa, K. Kitano, and S. Hamaguchi, “Effects of pH on bacterial inactivation in aqueous solutions due to low-temperature atmospheric pressure plasma application,” *Plasma Process. Polym.* **7**, 33 (2010).
- ³³R. Zhou, R. Zhou, P. Wang, Y. Xian, A. Mai-Prochnow, X. Lu, P. J. Cullen, K. Ostrikov, and K. Bazaka, “Plasma-activated water: Generation, origin of reactive species and biological applications,” *J. Phys. D* **53**, 303001 (2020).
- ³⁴A. Jo, H. M. Joh, T. H. Chung, and J. W. Chung, “Anticancer effects of plasma-activated medium produced by a microwave-excited atmospheric pressure argon plasma jet,” *Oxid. Med. Cell. Longevity* **30**, 4205640 (2020).
- ³⁵I.-E. Vlad and S. D. Anghel, “Time stability of water activated by different on liquid atmospheric pressure plasmas,” *J. Electrostat.* **87**, 284 (2017).
- ³⁶K. Oehmigen, M. Hähnel, R. Brandenburg, C. Wilke, K.-D. Weltmann, and T. von Woedtke, “The role of acidification for antimicrobial activity of atmospheric pressure plasma in liquids,” *Plasma Process. Polym.* **7**, 250 (2010).
- ³⁷D. X. Liu, Z. C. Liu, C. Chen, A. J. Yang, D. Li, M. Z. Rong, H. L. Chen, and M. G. Kong, “Aqueous reactive species induced by a surface air discharge: Heterogeneous mass transfer and liquid chemistry pathways,” *Sci. Rep.* **6**, 23737 (2016).
- ³⁸I. V. Schweigert, A. L. Alexandrov, and D. E. Zakrevsky, “Self-organization of touching-target current with ac voltage in atmospheric pressure plasma jet for medical application parameters,” *Plasma Sources Sci. Technol.* **29**, 12LT02 (2020).
- ³⁹K. Zhang, M. Zhao, D.-W. Sun, and B. K. Tiwari, “Correlation of plasma generated long-lived reactive species in aqueous and gas phases with different feeding gases,” *Plasma Sources Sci. Technol.* **32**, 045015 (2023).